Analysis of mechanical behavior of fiber-glass plastic with hole pattern using digital image correlation and acoustic emission methods

E. M. Strungar, D. S. Lobanov, E. A. Chebotareva, Y. V. Kochneva
Center of Experimental Mechanics, Perm National Research Polytechnic University, Russia
cem.spaskova@mail.ru, https://orcid.org/0000-0002-2246-8638
cem.lobanov@gmail.com, https://orcid.org/0000-0003-1948-436X
cem.chebotareva@mail.ru, https://orcid.org/0000-0002-6374-6964
yaroslavaviktorovna@gmail.com, http://orcid.org/0000-0002-2345-6790

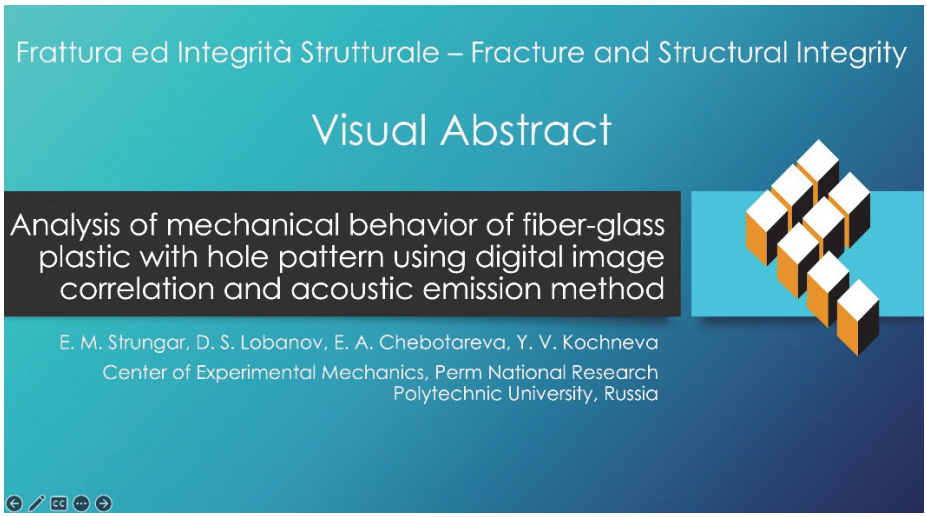

Citation: Strungar E.M., Lobanov D.S., Chebotareva E.A., Kochneva Y.V., Mechanical behavior of fiber-glass plastic with hole pattern using digital image correlation and acoustic emission methods, 68 (2024) 63-76.

Received: 21.11.2023
Accepted: 13.01.2024
Published: 18.01.2024
Issue: 04.2024

KEYWORDS. Digital Image Correlation method, Acoustic emission, Mathematical modeling, Stress concentrator, Open-hole, Fiberglass.

INTRODUCTION

The widespread use of polymer composites in all areas of aerospace, electronics, automotive energy and mechanical engineering provides a number of application advantages over metals. For the civil aviation industry, the integration of composite elements in a structure is accomplished by mechanical fastening. This process requires a large number of drilled holes for the positioning of rivets and bolts. Assembly is accomplished using fasteners. For isotropic materials such as steel, bolted connections are often preferred because of their practical construction. In research [1], the fatigue performance of 2024-T3 aluminum alloy sheet with varies staggered hole arrangement and multi-site damage was investigated, which includes the row spacing, column spacing and inter-crack directions. This study [2] investigated the net section resistance of HSS staggered bolted connections experimentally and numerically. However, due to the anisotropic

and brittle nature of materials in composites, bolt-induced stresses are redistributed differently, affecting the assumed limit states. In structures where composite components are bolted together [3-5], it is often necessary to introduce multi-start holes, it is necessary to perform parametric analysis of stresses taking into account multiple variations of hole configuration [6-10]. The importance of finite element mesh selection in modeling composites with stress concentrators is discussed in study [11], where models with different degrees of sampling are studied and the results of which model are closest to the experimental data are identified. In study [12], modeling of a composite (WFKC) with multiple holes was carried out and compared with the experiment. In non-staggered plates, the maximum stresses occur in the outermost holes [13-15]. In staggered hole arrangement, the fracture depends on the smallest cross-sectional area in the direction perpendicular to the plane axis. In study [16], 11 multi-hole configurations with different spacing and spacing between staggered and non-staggered arrangement of FRP holes were studied. In most cases, staggered holes demonstrated a staggered trajectory, while a series of non-staggered holes demonstrated a crack trajectory along the section plane.

It is not possible to consider a composite as a homogeneous body when solving problems aimed at investigating stress concentrations occurring near cracks, notches, various geometrical holes and technological defects having dimensions comparable to the characteristic size of the structure [17-19]. The research paper by Donald Cunningham, Kent A. Harris, Andrew J. and Bell [20] presents a study in which the effect of circular hole on tensile strength in pultruded staggered hole fiberglass is addressed. It may also be noted that this study [20] uses digital image correlation method. VIC-3D was used to evaluate two-dimensional strain fields on the surface of the specimens. The authors of the study claim that using the same net cross-sectional calculations as for steel, a ductile isotropic material, is not appropriate for FRP, a relatively brittle and often highly anisotropic material. This is particularly important when offset hole connections are used. The fracture of materials is always accompanied by the emission of elastic waves, which can be recorded using the acoustic emission method [21,22]. By analyzing such signals, it is possible to obtain information about the damage accumulation process as well as to identify the failure mechanisms in the material [23-30].

The stress distribution around the holes is evaluated using computational methods and experimental stress analysis. An important scientific direction includes experiments with the use of combined methods to study the fracture of composite objects with concentrators in the form of holes. In the studies of many authors [31-33] the prospect of joint use of video system of non-contact measurement and analysis of displacement and deformation fields for the analysis of mechanical behavior of composites, calculation methods, infrared thermal scanning systems and acoustic emission method is noted. The joint use of these methods is conditioned by the necessity of obtaining additional important information on determining the moment of damage initiation and its location, on defect propagation in the material.

Thus, the main purpose of the study is to comprehensively investigate the regularities of deformation processes, damage accumulation and fracture in polymer composite in stress concentration zones. Fiber-glass plastic STEF as a model material based on combined epoxy and phenol-formaldehyde resins was chosen as the study object.

MATERIAL, TOOLS AND METHOD

Tensile tests were performed on an Instron 5982 electromechanical testing system (100kN) under «rigid» loading with a constant speed of the movable gripper of 2 mm/min (for specimens with the same working zone), together with an optical video system for analyzing strain and displacement fields VIC-3D and a system for recording acoustic emission (AE) signals AMSY-6. The test and measurement systems were synchronized during testing using a 16-bit NI USB-6251 high-speed A/D converter unit.

The material used in this study is fiber-glass plastic STEF. This is a laminated reinforced fiberglass plastic obtained by hot pressing of glass fabrics impregnated with thermosetting binder based on combined epoxy and phenol-formaldehyde resins with sufficiently high mechanical characteristics. Fiber-glass plastic is used in insulation systems of large mechanisms and machines, hydro- and turbo generators, parts of electrical engineering. STEF is produced according to the Russian National Standard (GOST 12652). The specimen holes were drilled using vertical drills.

Video recording of the specimen deformation process was carried out using two Prosilica 50 mm cameras (resolution 4872 x 3248, 16 MP). The shooting frequency was 3 frames per second. The software of the Vic-3D video system provides the use of various correlation criteria for mathematical evaluation of digital image matching. The standardized sum of squares difference criterion with zero mean is used in this study because it is the least sensitive to illumination changes during the test, providing the best combination of time frame and accuracy of the results. During post-processing, the Lagrangian finite strain tensor was used for the calculation. The Oy axis is directed along the specimen (along the axis of load application), and the Ox axis is perpendicular to the loading axis in the plane of the specimen. The additional program module of the "virtual extensometer" video system was used to trace the mutual displacement of two points on the specimen surface with

respect to the applied force. The accuracy of the non-contact optical system is determined by the technical characteristics of lenses and digital cameras, namely the sensitivity of the matrix, resolution and allowable frame rate. The accuracy of the obtained experimental data is also affected by the specimen surface, configuration and calibration of the chambers. According to the test results given in [34], it was concluded that using the Vic-3D digital optical system it is possible to determine the strain with an accuracy comparable to that of a hinged extensometer, the maximum possible deviation from the true value being 0.15%.

Acoustic emission signals were recorded by the Vallen AMSY-6 system. One AE144A broadband sensor with a frequency range of 100-500 kHz and a preamplifier with a gain of 34 dB were used to record the signals. The sensor was attached to the specimen using a mounting system. The data sampling frequency was 10 MHz and the threshold value of AE signal registration was 40 dB. The energy parameter, duration of AE signals, and frequency of spectral maximum (Fast Fourier Transform characteristic) were used as informative parameters. The energy parameter of AE signals was calculated using a special program option in energy units (eu), 1 eu = 10^{-14} $B^2 \cdot c$.

The research program included mechanical uniaxial tensile tests of composite specimens 50 mm wide and 4 mm thick, with 1, 2 and 3 round holes of equal diameter d=6 mm (Fig. 1). A total of 2 samples of each geometry were tested. The scheme of staggered arrangement of holes on the specimen surface and geometrical dimensions are presented in Tab. 1. This table provides data on g - gage distance (across specimen; horizontal in Fig. 1), s - stagger pitch (along specimen; vertical in Fig. 1) and the net section area - $A_{n,ns}$ (mm^2) - defined by Eq 1. Elastic boundary value problems for uniaxial tension of flat plates with an applied system of holes were solved using the SIMULIA Abaqus software application package. The boundary conditions were selected in such a way as to ensure the equality of the calculated external load and the experimental load. For each of the plates, a sampling area was considered, which was further approximated by quadrilateral and triangular finite elements. The specified meshes were not free, but made regular, without local densification.

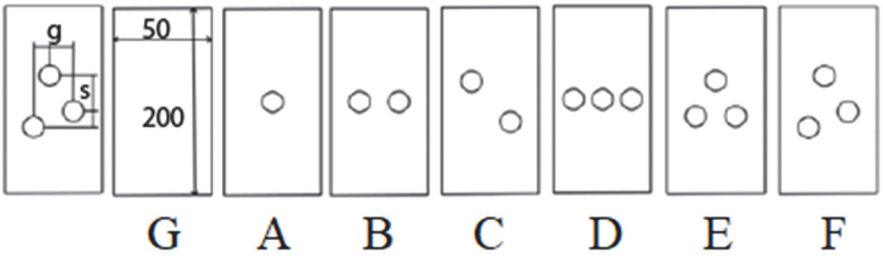

Figure 1: Sample geometry

Schemes	G	A	B	C	D	E	F
N	0	1	2	2	3	3	3
g (mm)	–	–	14.98	14.88	14.88	15.01	g_1=19.50 g_2=14.90
s (mm)	–	–	–	14.78	–	15.03	s_1=20.29 s_2=15.29
$A_{n,ns}$ (mm^2)	200	184.67	161.59	157.7	134.31	140.05	131.90

Table 1: Sample geometry.

RESULTS AND DISCUSSION

Load diagrams

Fig. 2, a shows pairs of loading diagrams for each scheme of FRP specimens. According to the test results, it can be concluded that the bearing capacity of the material for schemes A, B, C, E, F decreased by 43-47%, these limits are marked in the figure by blue dotted lines (Fig. 2, a). Expectedly, for scheme D the reduction turned out to be much larger, amounting to 65%. For the groups of specimens, the scatter in average values of ultimate stresses amounted to 160.30±6.15MPa (Fig.2, b) with the coefficient of variation V=3.84%. The results of tensile tests were present in Tab. 2.

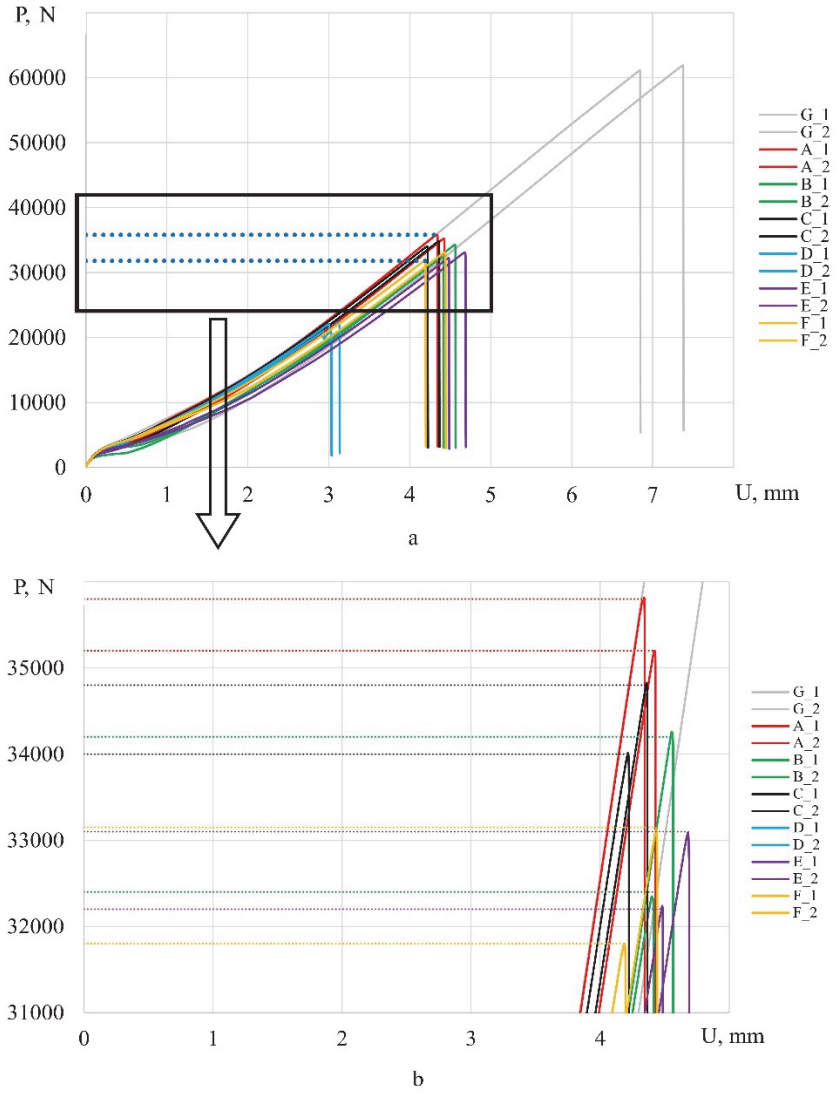

Figure 2: Loading diagrams of specimens of each scheme (a), scatter of maximum/minimum values of ultimate load for schemes A, B, C, E, F (b).

Mech. prop.\ Schemes	G	A	B	C	D	E	F
Max load, kN	61.50	35.50	33.30	34.40	21.70	32.70	32.50
Max. displacement, mm	7.12	4.39	4.50	4.30	3.08	4.59	4.32
Ultimate Stress, MPa	295.50	168.50	157.50	165.00	103.50	154.00	156.50

Table 2: Results of tensile testing of FRP specimens.

The plates were subjected to static tension, and the properties were determined on solid specimens without a concentrator. Mechanical characteristics of the samples: $E_{11}= E_{22}= E_{33}= 24,6$ GPa; $\nu_{12}= \nu_{13}= \nu_{23}=0,128$; $G_{12}= G_{13}= G_{23}=2,9$ GPa.

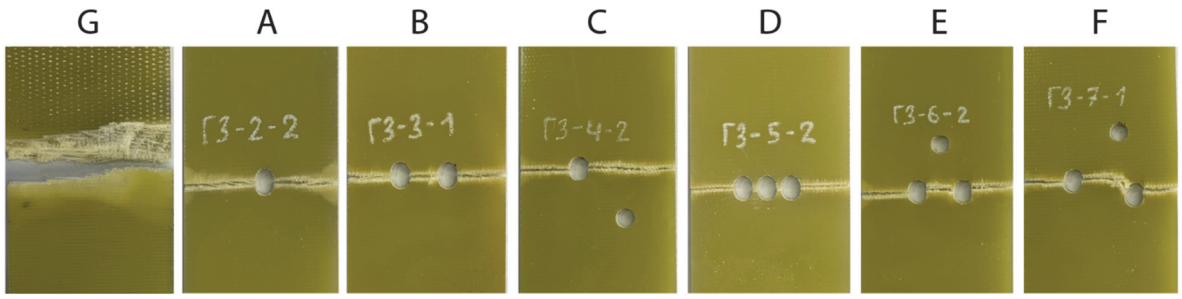

Figure 3: Crack path.

Analyzing the fracture patterns of specimens with different hole patterns (Fig. 3) it can be noted that the fracture of specimens of patterns A and C occurs through one hole in the cross-section, and for patterns B, E and F the «path» of fracture (breakaway crack) passes through two holes, and the bearing capacity of FRP plates with patterns A, C and B, E, F is comparable.

Inhomogeneous displacement and strain field analysis

To evaluate the displacement and deformation fields on the specimen surface, a non-contact optical video system Vic-3D was used, the mathematical apparatus of which is based on the DIC method. Prior to testing, a fine coating must be applied to the surface before the specimen is loaded. With the help of which the reliable determination of displacements is provided and the contrast of the studied surface is increased. In this study, a combination of black and white dots was applied to the surface of the sample using spray paint.

Fig. 4 shows the longitudinal strain epures (vertical direction in the images) across the full 50 mm width of the specimen through each hole along the line L. This results in an average of 170 data points each. The holes produce a discontinuity in the data along each 8 mm wide line, taking into account the edge effect. In this case, the Oy axis is directed along the specimen (along the tensile axis) and the Ox axis is perpendicular to the loading axis in the plane of the specimen. For clarity, the strain data along each line are plotted on photographs of the specimen at the same instant of time and correspond to P_u. From these data, the maximum strains near the holes can be obtained (ε_{yy}).

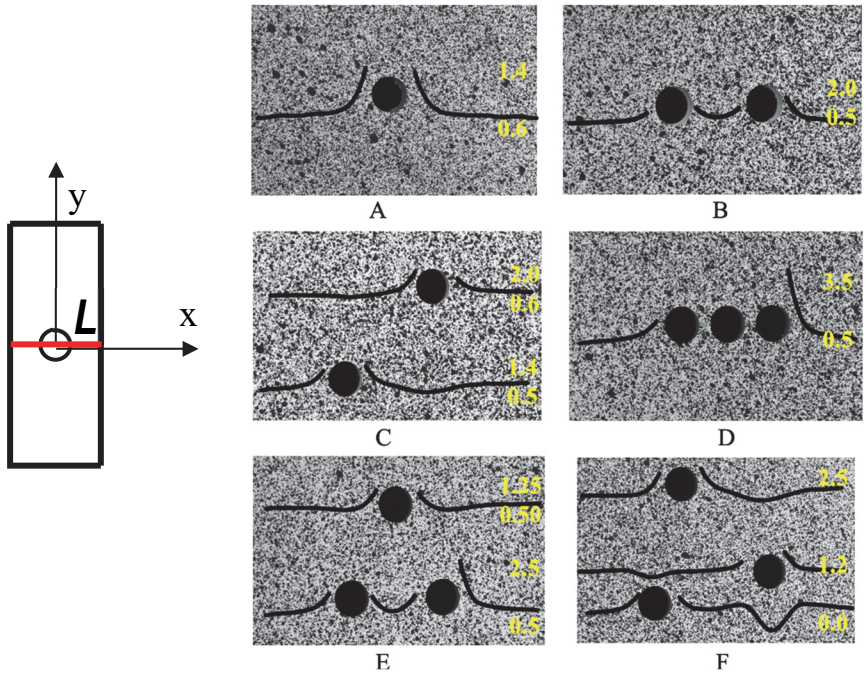

Figure 4: Longitudinal strain epures on the surface of specimens with a system of holes at maximum load.

The given longitudinal strain fields at maximum load clearly demonstrate the disposition of localization of defects that lead to complete fracture of the specimen (Fig. 5).

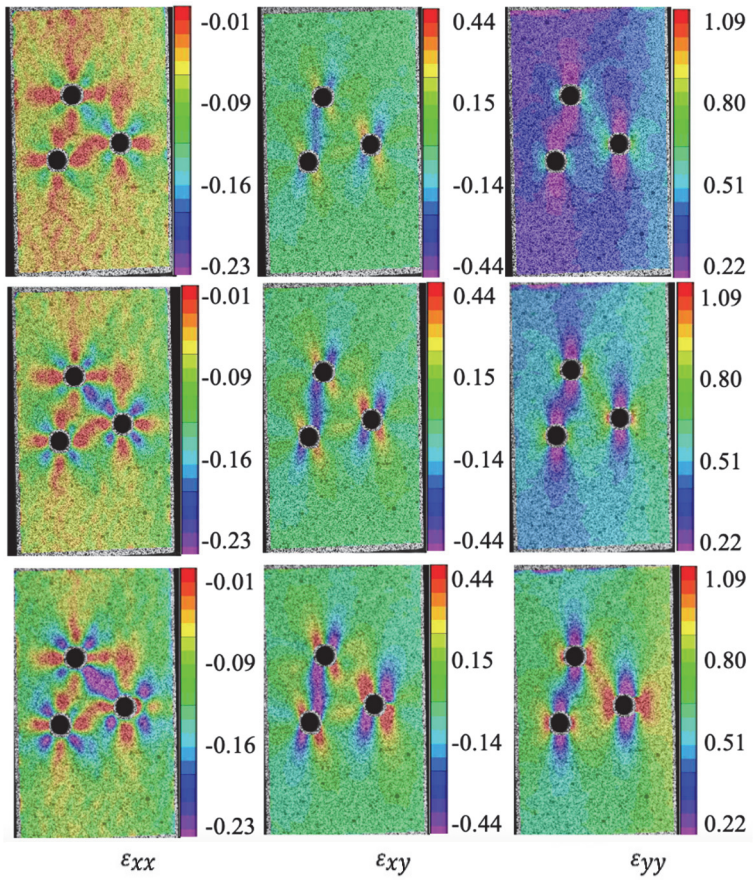

Figure 5: Inhomogeneous fields of transverse, shear and longitudinal strains on the specimen surface F.

According to the results obtained, it can be noted that in all cases the fracture of the specimen occurred without the development of a zigzag crack. Considering this geometry of staggered hole arrangement, it can be concluded that two additional holes did not affect the fracture process. According to the presented inhomogeneous fields, it is possible to ascertain the presence and growth of strain level concentration around the hole, which in turn leads to crack propagation and subsequent fracture of the specimen. In all cases, the fracture of the specimens occurred in the area where a localized maximum of longitudinal deformation is observed. The material strain process is inhomogeneous, on the surface of the specimen there are localized strain zones in the form of longitudinal strips, which, in turn, reflect the structure of the material.

Comparison of Numerically and Experimentally Obtained Strain Fields and Load Diagrams

Elastic boundary value problems for uniaxial tension of flat plates with an applied system of holes were solved using the SIMULIA Abaqus software application package.

Setting of the elastic task is supplemented by boundary conditions, which were selected in such a way as to ensure equality of the calculated external load to the experimental one. The convergence of the tasks is determined by the maximum normal stress σ_{22} on different meshes. The deviation σ_{22} from the previous value was calculated by the formula $\delta^i = \frac{\sigma_{22}^{(i)} - \sigma_{22}^{(i-1)}}{\sigma_{22}^{(i)}} * 100$. For each of the plates, the sampling area was considered, which was further approximated by quadrilateral and triangular finite elements (FEs); the given meshes were not free, but were made regular, without local densification. According to the results of the convergence of the tasks, the most optimal mesh size for each plate, regardless of the shape of the finite element, had a finite element with linear size of 0.15 c.u. In order to select a suitable mesh for the most precision description of the strain fields, the mean component values ε_{yy} in the Vic-3D digital optical system were compared with the mean component ε_{22} values in the elastic task solved in the software application package for the quadrilateral and triangular element (Tab. 3). In this approach, averaging of strain components was done over the area -

working part of the specimen. The comparison showed that the triangular finite element can be effective in describing certain configurations.

Schemes	ε_{22}, %		
	Vic-3D	Quadrilateral element	Triangular element
A	0.71	0.70	0.73
B	0.61	0.71	0.65
C	0.70	0.65	0.67
D	0.49	0.46	0.43
E	0.65	0.62	0.64
F	0.64	0.64	0.65

Table 3: Finite element selection.

Thus, quadrilateral finite elements were used for plates with a single (N=1) circular cutout (A); with circular cutouts (N=3) located on the same line (D); with a staggered arrangement of (N=3) concentrators (F); and triangular finite elements for all others. Experimental data were used to analyze the strain fields on plates with the applied hole pattern and compared with the results of numerical calculations (Fig. 6). It can be concluded from the figure that the strain fields on these structures are quantitatively and qualitatively similar and well matched.

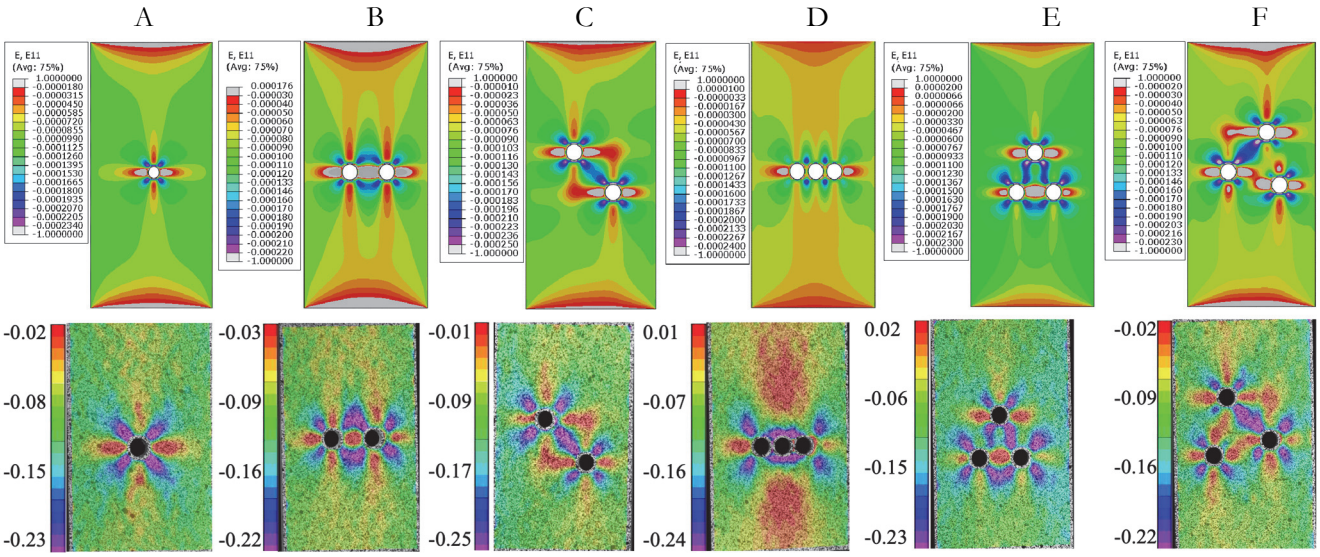

Figure 6: Comparison of calculated and experimental deformation fields εxx.

Analysis of acoustic emission signals

Based on the results of acoustic emission signal registration, parametric analysis of experimental data was carried out. First of all, the level of cumulative energy of AE signals was evaluated, which reflects the degree of damage accumulation in the material (Fig. 7). It can be noted that the character of cumulative energy growth in all types of specimens is similar: weak responses were recorded during the test, and then a sharp jump in energy at specimen fracture. It is also possible to single out specimen D. Before the maximum peak, a preliminary jump in cumulative energy was recorded. It is associated with the material fracture between the holes in the specimen.

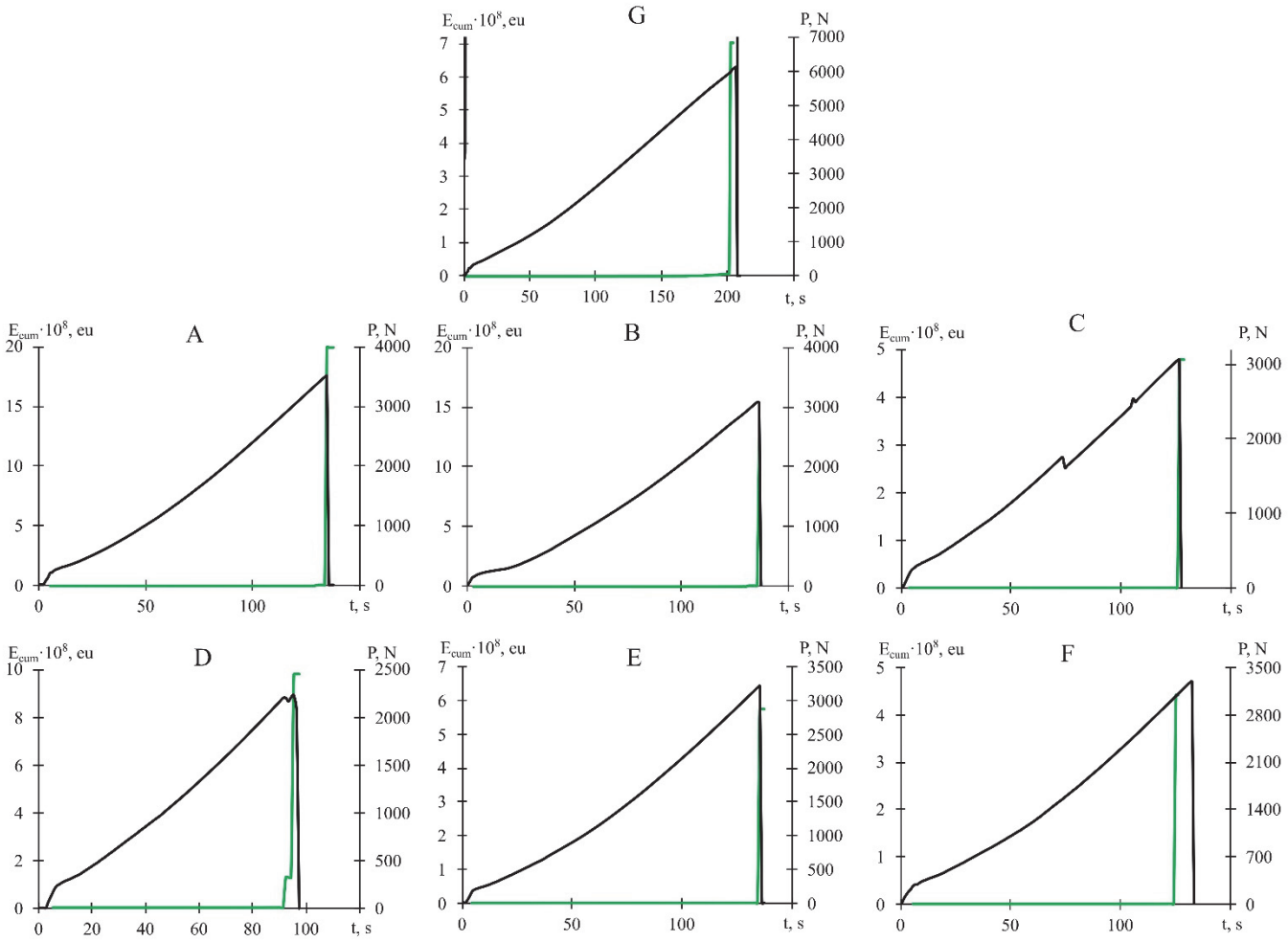

Figure 7: Time dependence diagrams of the cumulative energy of AE signals together with the loading diagrams.

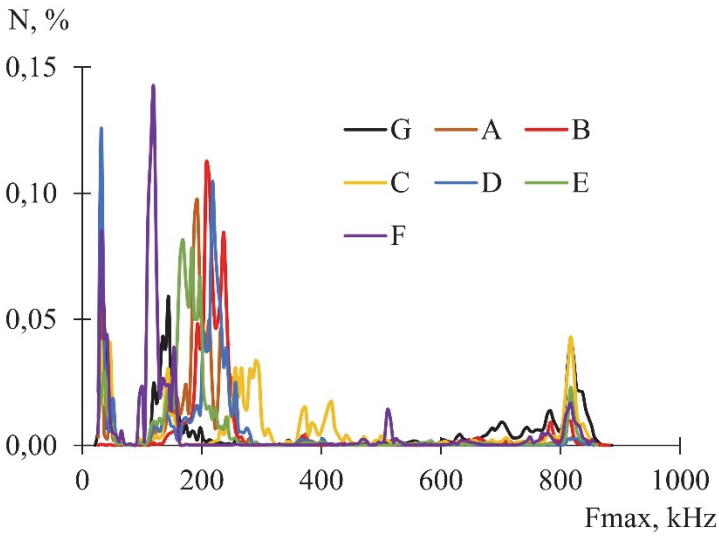

Figure 8: Histogram of the frequency distribution of the spectral maximum.

The peak frequencies of AE signals were also analyzed. Histograms of the frequency distribution of the spectral maximum frequencies of the signals were plotted (Fig. 8). Three frequency ranges can be distinguished from the data for all specimens: 100-310 kHz, 350-550 kHz, 700-900 kHz. Since during the preliminary calibration of the system it was found out that the

signals with frequency lower than 100 kHz are noise produced by the machine, these signals were not taken into account in further analysis. From the peak frequency ranges it is possible to draw conclusions about the fracture mechanisms in the material. Thus, low frequencies correspond to matrix cracking, medium frequencies correspond to delamination, and high frequencies correspond to fiber fracture. In general, there is no consensus that a particular frequency corresponds to a particular type of fracture. However, some typical frequency ranges corresponding to different types of damage are widely accepted by researchers [25, 26, 30].

From the histogram data, it can be seen that the peak frequencies of the signals are characteristic of all types of specimens. However, in order to estimate them more accurately, the dependences of peak frequencies on time were plotted (Fig. 9). The figure shows that the number of signals in the high and middle frequency range differs between different specimen types. For quantitative evaluation, the signals in the previously selected ranges were selected. The results are shown in Fig. 10.

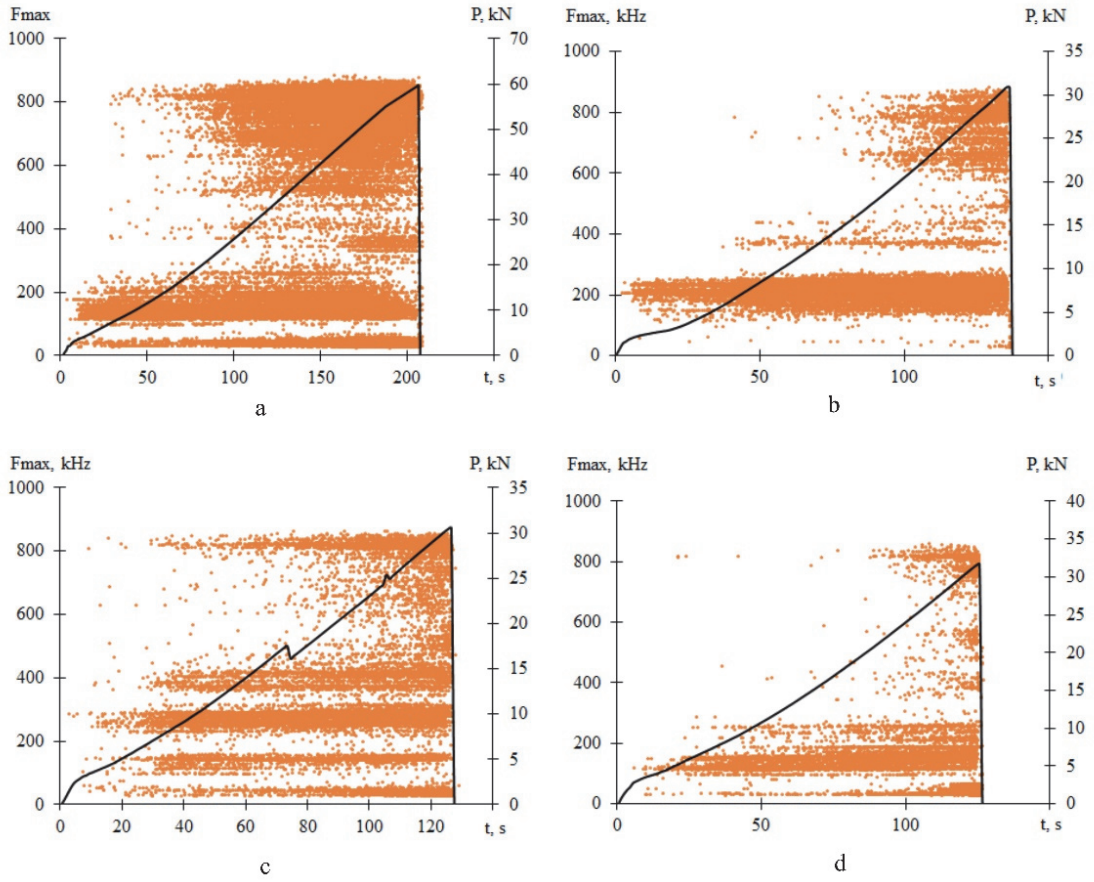

Figure 9: Time dependence diagrams of peak frequencies of AE signals of samples G (a), B (b), C (c), F (d).

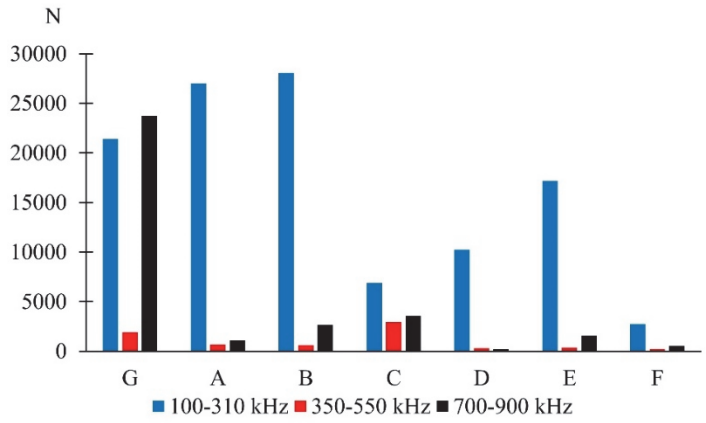

Figure 10: Histograms of the number of AE signals in different frequency ranges for each sample type.

From the results, reflected in the histogram, it can be seen that the signals in the low-frequency range are significantly predominant in most types of specimens, from which it can be concluded that the material fracture occurred as a consequence of matrix cracking. In specimen G (specimen without an open hole), the number of signals in the high-frequency range is higher than in the low-frequency range. In type 4 specimen, the number of signals corresponding to matrix cracking is also predominant, but not by several orders of magnitude as in the other specimens. It can be assumed that in most of the specimens, the matrix worked predominantly during loading, and the signals due to the fracture of which were recorded in greater number. However, in specimen G the fibers also worked during loading along with the matrix. And specimen C lost its bearing capacity not only due to matrix cracking, but also due to delamination and fiber rupture. The external appearance of the destroyed samples (Fig. 11) confirms the conclusions drawn from the analysis of acoustic emission signals.

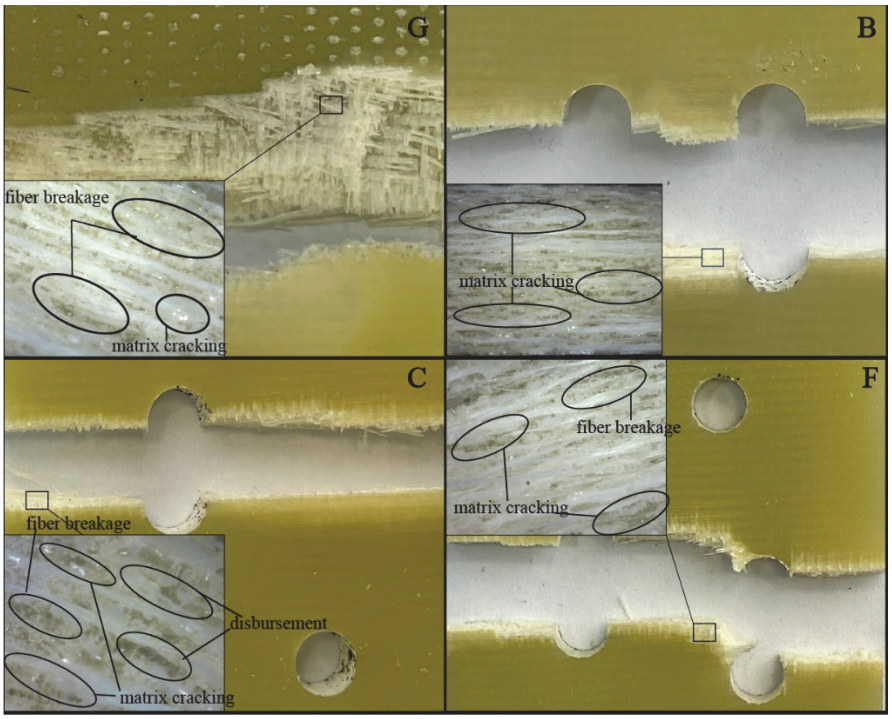

Figure 11: Photo of specimens G (a), B (b), C (c), F (d) after fracture.

EFFECT OF STAGGERING HOLES

The current American Specification AISC [35] (ANSI/AISC 360-22) requires that all potential fracture planes along the line of holes perpendicular to the external load be analyzed.

$$An, ns = Ag - Nht \tag{1}$$

Where Ag=bt – total cross-sectional area of the part, N - number of holes, h - diameter of holes, t - thickness, b - width. However, for a staggered configuration in an isotropic material, this estimate is an overestimate and does not account for the increase in strength due to the diagonal path (sometimes called zigzag path) between neighboring holes resulting from the step (s) of the connection. Consequently, a value is added for each neighboring hole subtracted (ANSI/AISC 360-22 Section B4.3b) $s^2/4g$ (where s - pitch, and g - gage of the hole pattern):

$$An = Ag - Nht + t\sum(s^2 / 4g) \tag{2}$$

A comparison of the ultimate capacity of solid specimen and specimens with the hole system on the same line (s=0) reveals the strength reduction associated with the presence of holes. The observed strength reduction factor k for the presence of holes is presented in Tab. 4. For the specimen with the number of holes $N = 3$, the reduction in ultimate capacity was 65%. In Tab. 5, the « Observed effect of stagger » is the ratio of the observed fracture stress for the case with staggered arrangement to the case without staggered arrangement (i.e. $F_u/F_{u,s=0}$). The « Prescribed effect of stagger » is the ratio of the cross-sectional area calculated from Eqn. (2) to the area calculated from Eqn. (1), the difference of which effectively isolates the member $s^2/4g$ (i.e., $A_n/A_{n,ns}$).

Schemes	Number of concentrators at d=6 mm, N	Gage g, mm	Capacity P_u, kN	Strength $F_u=P_u/A_{n,ns}$, MPa	Observed strength reduction Factor $F_u/F_{u\ Schemes\ A}$, k
G	–	–	61.9	310	–
A	1	–	35.5	192	0.62
B	2	14.98	33.3	206	0.67
D	2	14.99	21.7	162	0.52

Table 4: Specimens capacity and strength reduction factor (k) in the presence of holes located on the same line (testing of specimens in longitudinal direction).

Schemes	Number of concentrators at d=6 mm, N	Gage g, mm	Pitch s, mm	Capacity P_u, kN	Strength $F_u=P_u/A_{n,ns}$, MPa	Observed effect of stagger $F_u/F_{u,s=0\ Schemes\ B}$	Prescribed effect of stagger $A_n/(A_{n,ns})$
C	2	14.88	14.78	34.4	219	1.04	1.10
E	3	15.01	15.03	32.7	235	1.14	1.20
F	3	g_1=19.50 g_2=14.90	s_1=20.29 s_2=15.29	32.5	249	1.21	1.29

Table 5: Capacity of specimens and effect of staggered arrangement.

For N=3 staggered arrangement (E), the strength of the tested specimens is higher than the strength value for similar specimen without staggered hole arrangement (D). At no value of s there was no fracture of specimens with staggered arrangement of holes according to the classical «zigzag» pattern. In determining the critical section, among the different paths, the one that gives the lowest value after subtracting the holes is chosen. Based on the «Observed effect of stagger» (Tab. 5), it is obvious that the $s^2/4g$ member does not make sense to add to Eqn. (1) when calculating the open-hole capacity for FRP specimens with staggered hole pattern, regardless of the step (s). The calculation showed that the critical areas excluding the $s^2/4g$ member are the smallest values and were: C – 36,41 mm, E – 22,83 mm, F – 23,69 mm.
Tab. 6 summarizes the strains that were obtained using DIC for each specimen shown in Tab. 1. The average net strain section (ε_{avg}) is calculated using Eqn. (3) and represents the expected uniform strain in the material if the holes had no stress-increasing effect.

$$\varepsilon_{avg} = \alpha P_u / A_{n,ns} E \tag{3}$$

where αP_u - is the fraction of the ultimate load at which the strain is calculated, $A_{n,ns}$ is determined by Eqn. (2), and E=24,6 GPa (Tab. 2) for a 4 mm thick plate.

Schemes	Number of concentrators at d=6 mm, N	g, mm	s, mm	Specimen width, b	Specimen thickness, t	$A_{n,ns}$, mm^2	P_u, kN	gage line	α	ε_{avg}	ε_{max}	$\varepsilon_{avg}/\varepsilon_{max}$
G	–	–	–	49.89	4.21	210	61.5	–		–	–	–
A	1	–	–	49.97	4.2	185	35.5	–		0.0078	0.0133	0.59123
B	2	14.98	–	49.88	4.25	162	33.3	–		0.0081	0.0194	0.4172
C	2	14.88	14.78	49.92	4.17	158	34.4	Upper Lower	1	0.0089 0.0089	0.0188 0.0140	0.4747 0.6369
D	3	14.99	–	49.86	4.21	134	21.7	–		0.0063	0.0339	0.1854
E	3	15.01	15.03	49.92	4.32	140	32.7	Upper Lower		0.0096 0.0096	0.0133 0.0246	0.7202 0.3892
F	3	g_1=19.50 g_2=14.90	s_1=20.29 s_2=15.29	49.88	4.16	132	32.5	Upper Medium Lower		0.0102 0.0102 0.0102	0.0123 0.0126 0.0249	0.8233 0.8088 0.4072

Table 6: Strain data obtained using DIC.

The average ratio of the average net section strain to the recorded strain at the edge of each hole is approximately $\varepsilon_{avg}/\varepsilon_{max}$=0,56. This indicates that the stress intensity factor associated with these holes is approximately K=1,79.

Conclusion

As a result of the study, new experimental data on the regularities of the processes of damage accumulation and fracture of composite plates with a hole pattern have been obtained:
- according to inhomogeneous fields, it is possible to ascertain the presence and growth of strain level concentration around the hole, which in turn leads to crack propagation and subsequent fracture of the specimen. In all cases the specimen fracture occurred without development of a zigzag crack, two additional holes did not affect the fracture process. Experimental data were used to analyze the strain fields on plates with the applied hole pattern and compared with the results of numerical calculations. The strain fields on these structures are quantitatively and qualitatively similar and well matched. The most accurate description of the strain fields does not require a finer finite element mesh. The degree of sampling of the area is the same and its change, including the shape of the finite element, leads to the deterioration of numerical calculations;
- based on the results of the analysis of acoustic emission signals, the ranges of peak frequencies corresponding to the fracture mechanisms in the material were identified. It was concluded that the geometry of the hole pattern had an insignificant effect on the fracture mechanisms, the specimens lost their load-bearing capacity mainly due to matrix cracking. Similar pattern of damage accumulation in all types of specimens was also noted:
- there is a consistent strength reduction associated with the drilled holes provided. To calculate of laminate the cross-sectional area in staggered or non-staggered arrangements the stagger pitch (along specimen; vertical in images) gage distance (across specimen; horizontal in images) ratio must be omitted. The pitch value can be at which the critical section ceases to be and can be a different range of pitch values will result in the formation of a «staggered» joint.
The test results show that, unlike isotropic materials, the use of a staggered hole arrangement on STEF material does not provide an advantage in strength performance. The authors hypothesize that the degree of anisotropy of the material will impact the conclusions presented. Further studies by varying the g and s ratios need to be conducted.

Acknowledgement

This work was carried out with the support of the Russian Science Foundation (Project No 22-79-00113 (https://rscf.ru/project/22-79-00113/») at the Perm National Research Polytechnic University.

REFERENCE

[1] Cunningham, D., Harries, K. A., Bell, A. J. (2015). Open-hole tension capacity of pultruded GFRP having staggered hole arrangement, J. Engineering Structures., 95, pp. 8–15. DOI: 10.1016/j.engstruct.2015.03.042.

[2] Lin, X. M., Yam, M. C. H., Chung, K. F., Ke, K. and He, Q. (2021). Experimental and numerical study on net section resistance of high strength steel staggered bolted connections, J. Engineering Structures., 247(113111). DOI: 10.1016/j.engstruct.2021.113111.

[3] Alaa, A., Hesham, M., Hani, A., Hossam, M., (2020). Deformation and load transfer analysis of staggered composite-steel lap joints subjected to progressive damage, J. Engineering Structures., 215. DOI: 10.1016/j.engstruct.2020.110690.

[4] Xin, L., Zhiyong, T., Lechen, W., Jian, Z., Zhen, X., Haibo, L. (2020). Experimental investigations of bolted, adhesively bonded and hybrid bolted/bonded single-lap joints in composite laminates, J. Materials Today Communications, 24. DOI: 10.1016/j.mtcomm.2020.101244.

[5] Xutong, Z., Junfeng, H., Rui, Q., Yifan, W., Sudong, Y., Yinyuan, H., Zhou, C., Dingding, C., Siqi, Z., Felix, E., Jingxuan, M., Wenlong, L. (2023). Experimental and numerical research on opening size effect of novel short fiber reinforced composite laminates, J. Results in Physics., 46. DOI: 10.1016/j.rinp.2023.106303.

[6] Yue, L., Bernd, Z., (2013). Stress Concentration and Failure of Perforated CFRP Lamella under Unidirectional Tension. Conference: Conference on Smart Monitoring Assessment and Rehabilitation of Civil Structures, Instanbul, Turkey.

[7] Jipeng, Z., Wen, Y., Yuan, Z., Yue, W. (2021). Effect of Hole Arrangement on Failure Mechanism of Multiple-Hole Fiber Metal Laminate under On-Axis and Off-Axis Loading, J. Materials., 14(19). DOI: 10.3390/ma14195771.

[8] Oudad, W., Bouzitouna, W.N., Noureddine, D., Mohamed, B. (2023). Failure behavior of a notched plate repaired by a hybrid repair technique (Stop hole bonded composite), J. Journal of the Brazilian Society of Mechanical Sciences and Engineering. DOI: 10.21203/rs.3.rs-2994646/v1.

[9] Donald, C., Kent, A. H., Andrew, J. B. (2015). Open-hole tension capacity of pultruded GFRP having staggered hole arrangement, J. Engineering Structures., 95, pp. 8–15. DOI: 10.1016/j.engstruct.2015.03.042.

[10] Chen, F., Jin, X. (2023). Experimental and Modeling Study of Open-Hole Composite Laminates Under Tension, Proceedings of the 10th Chinese Society of Aeronautics and Astronautics Youth Forum, Singapore, pp. 1–7.

[11] Boyang, C., Tay, T.E., Pedro, B., Silvestre, P. (2013). Numerical analysis of size effects on open-hole tensile composite laminates, J. Composites Part A Applied Science and Manufacturing., 47(1), pp. 52–62. DOI: 10.1016/j.compositesa.2012.12.001.

[12] Khairi, S., Hilton, A. (2017). Stress distribution study on multi-holes configurations in woven fabric kenaf composite plates. IOP Conference Series Materials Science and Engineering, Johor Bahru, Malaysia.

[13] Strungar, E.M., Lobanov, D.S., Wildemann, V.V. (2021). Evaluation of the Sensitivity of Various Reinforcement Patterns for Structural Carbon Fibers to Open Holes during Tensile Tests, J. Polymers., 13(24). DOI: 10.3390/polym13244287.

[14] Strungar, E. M., Wildemann, V. E. (2020). Inelastic deformation and destruction of fiber-laminated polymer composites in stress concentration zones, J. Frattura ed Integrità Strutturale., 53, pp. 406–416. DOI: 10.3221/IGF-ESIS.53.31.

[15] Strungar, E. M., Lobanov, D.S. (2020). Mathematical data processing according to digital image correlation method for polymer composites, J. Frattura ed Integrità Strutturale., 54, pp. 56–65. DOI: 10.3221/IGF-ESIS.54.04.

[16] Khairi, S., Hilton, A. (2017). XFEM Modelling of Multi-holes Plate with Single-row and Staggered Holes Configurations. MATEC Web of Conferences.

[17] Morten, G.O., Ibbotson, A.R., Roux, O.L., Prior, A.M. (2011). Virtual testing of aircraft structures, J. CEAS Aeronautical., 1(1), pp. 83–103. DOI: 10.1007/s13272-011-0004-x.

[18] Karpov, E.V. (2002). Stress concentration and fracture near circular holes in composite structural elements dissertation of candidate of physical and mathematical sciences.

[19] Panin, V.E., Likhachev, V.A., Grinyaev, Y.V. (1985). Structural levels of deformation of solids, Moscow, Nauka.

[20] Cunningham, D., Harries, K.A., Bell A.J. (2015). The art of writing a scientific article, J. Experimental Mechanic., 38(1), pp. 8–15. DOI: 10.1016/j.engstruct.2015.03.042.

[21] Pan, T., Zheng, Y., Zhou, Y., Luo, W., Xu, X., Hou, C., Zhou, Y. (2023). Damage pattern recognition for corroded beams strengthened by CFRP anchorage system based on acoustic emission techniques, J. Construction and Building Materials., 406. DOI: 10.1016/j.conbuildmat.2023.133474.

[22] Xu, J., Wang, W., Han, Q., Liu, X. (2020). Damage pattern recognition and damage evolution analysis of unidirectional CFRP tendons under tensile loading using acoustic emission technology, J. Composite Structures., 238. DOI: 10.1016/j.compstruct.2020.111948.

[23] Nair, A., Cai, C.S., Kong, X. (2019). Acoustic emission pattern recognition in CFRP retrofitted RC beams for failure mode identification, J. Composites Part B: Engineering., 161, pp. 691–701. DOI: 10.1016/j.compositesb.2018.12.120.
[24] Johnson, M. (2002). Waveform based clustering and classification of AE transients in composite laminates using principal component analysis, J. NDT and E International., 35(6), pp. 367–376. DOI: 10.1016/S0963-8695(02)00004-X.
[25] Tayfur, S., Alver, N., Tanarslan, H.M., Ercan, E. (2018). Identifying CFRP strip width influence on fracture of RC beams by acoustic emission, J. Construction and Building Materials., 164, pp. 864–876. DOI: doi.org/10.1016/j.conbuildmat.2018.01.189.
[26] Bannikov, M., Sazhenkov, N., Balakirev, A., Sazenkov, N., Uvarov, S., Bayandin, Y., Nikitiuk, A., Nikhamkin, M., Naimark, O. (2022). Acoustic emission phase analysis of damage-failure transition staging in composite materials, J. Procedia Structural Integrity., 41, pp. 518–526. DOI: 10.1016/j.prostr.2022.05.059.
[27] Liu, Y., Zhang, L., Li, Z., Chen, Z., Huang, K., Guo, L. (2023). Investigation on damage evolution of open-hole plain woven composites under tensile load by acoustic emission signal analysis, J. Composite Structures., 305. DOI: 10.1016/j.compstruct.2022.116481.
[28] Rishikesan, V., Bhagyesh, C., Arunachalam, N J. (2021). Characterisation of drilling-induced damage in GFRP Honeycomb Sandwich Composites using Acoustic Emission, J. Procedia Manufacturing., 53, pp. 664–672. DOI: 10.1016/j.promfg.2021.06.066.
[29] Sawan, A.H., Walter, M.E., Marquette B. (2015). Unsupervised learning for classification of acoustic emission events from tensile and bending experiments with open-hole carbon fiber composite samples, J. Composites Science and Technology., 107, pp. 89–97. DOI: 10.1016/j.compscitech.2014.12.003.
[30] Özaslan, E., Yetgin, A., Acar, B., Güler, M.A. (2021). Damage mode identification of open hole composite laminates based on acoustic emission and digital image correlation methods, J. Composite Structures., 274. DOI: 10.1016/j.compstruct.2021.114299.
[31] Strungar, E.M., Lobanov, D.S., Zubova, E. M., Babushkin, A.V. (2020). Analysis of the mechanical behavior of spatially reinforced composites with open holes. IOP Conf. Series: Materials Science and Engineering, Novosibirsk, Russia,
[32] Lobanov, D., Yankin, A., Mullahmetov, M., Chebotareva, E., Melnikova, V. (2023). The Analysis of Stress Raisers Affecting the GFRP Strength at Quasi-Static and Cyclic Loads by the Theory of Critical Distances, Digital Image Correlation, and Acoustic Emission, J. Polymers., 15(9). DOI: 10.3390/polym15092087.
[33] Lobanov, D.S., Slovikov, S.V., Lunegova, E.M. (2023). Influence of internal technological defects on the mechanical properties of structural CFRP, J. Frattura ed Integrita Strutturale, 17(65), pp. 74–87. DOI: 10.3221/IGF-ESIS.65.06.
[34] Lobanov, D. S., Strungar, E. M., Zubova, E. M., Wildemann, V. E. (2019). Studying the Development of a Technological Defect in Complex Stressed Construction CFRP Using Digital Image Correlation and Acoustic Emission Methods, J. Russian Journal of Nondestructive Testing., 55(9), pp. 632–638. DOI: 10.1134/S1061830919090031.
[35] AISC. (2022). Specification for structural steel buildings. ANSI/AISC 360-22, Chicago, American Institute for Steel Construction.